Journal of Biomimetics, Biomaterials and Biomedical Engineering
ISSN: 2296-9845, Vol. 73, pp 113-121
doi:10.4028/p-7wWG1w

Submitted: 2026-01-09
Accepted: 2026-02-23
Online: 2026-07-30

Compaction Behavior of Stainless Steel/Carbamide Mixtures in Porous Scaffold Fabrication *via* Space Holder Method

Ajie Prasojo[1,a], Muslim Mahardika[1,2,b], Rini Dharmastiti[1,2,3,c], Jie Zhou[4,d] and Budi Arifvianto[1,2,d] *

[1]Departement of Mechanical and Industrial Engineering, Faculty of Engineering, Universitas Gadjah Mada, Jl. Grafika 2 Yogyakarta 55281, Indonesia

[2]Centre for Innovation of Medical Equipment and Devices (CIMEDs), Faculty of Engineering, Universitas Gadjah Mada, Jl. Teknika Utara Yogyakarta 55281, Indonesia

[3]Biomedical Engineering Program, Graduate School, Universitas Gadjah Mada, Jl. Teknika Utara Yogyakarta 55281, Indonesia

[4]Department of Biomechanical Engineering, Faculty of Mechanical Engineering, Delft University of Technology, Mekelweg 2, 2628 CD Delft, The Netherlands

[a]ajieprasojo@mail.ugm.ac.id, [b]muslim_mahardika@ugm.ac.id, [c]rini@ugm.ac.id, [d]j.zhou@tudelft.nl, budi.arif@ugm.ac.id.

*Corresponding author: Budi Arifvianto

Keywords: powder metallurgy; compaction; stainless steel 316L; scaffold; space holder method

Abstract. The medical grade 316L stainless steel has been widely used for biomedical implants, including bone tissue engineering scaffolds due to its excellent mechanical properties and biocompatibility. The space holder method offers a promising approach to producing highly porous 316L stainless steel scaffolds. However, several challenges in the implementation of this method remain unresolved, particularly the difficulties in controlling the geometrical changes of space holder particles during the compaction of stainless steel/carbamide powder mixtures, leading to inability to control pore characteristics of the scaffolds produced. In this study, the compaction behavior of stainless steel/carbamide powder mixtures was investigated to understand the interactions between metal particles and space holder particles in the preparation of porous stainless steel scaffolds. The impacts of key process parameters on the green density, such as the specific net energy applied during the process and the yield pressure derived from loading-unloading compression cycles, were analyzed with the aid of the Heckel model. The study provides useful insights into these relationships, facilitating the optimization of the compaction process to achieve desired scaffold architecture and contributing to consistent fabrication of porous 316L stainless steel scaffolds.

Introduction

Metallic scaffolds have recently gained prominence as a key element in bone tissue engineering, as they provide the template for bone tissue formation and stimulate bone tissue regeneration. It is attributed primarily to their porous architecture, which supports nutrient transport, bone ingrowth, and uniform stress distribution between the implant and host bone with significantly reduced stress shielding [1-4]. Various fabrication techniques of metallic scaffolds have been developed, including powder metallurgy, freeze casting, the space holder method, and additive manufacturing. Among these, the space holder method stands out for its superior control over pore size, shape, and distribution, as compared to conventional powder metallurgy [5, 6]. It also offers greater flexibility in selecting the metals, alloys or metal-matrix composites for scaffold construction. In principle, the process of scaffold fabrication with the space holder method involves mixing metallic matrix powders with space holder particles, compacting the blended powders into a green body, removing the space holder and sintering the brown body. The resulting pore morphology and mechanical properties are significantly influenced by the choice of materials, the volume fraction of space holder used, and the compaction parameters applied during processing [5, 7, 8].

The medical grade 316L stainless steel (SS316L) has been widely used as a scaffold material owing to its biocompatibility, high strength, corrosion resistance, and ductility [9, 10]. Meanwhile, carbamide has been commonly employed as a space holder material, as it can be readily removed, typically through water leaching, without leaving harmful residues behind [4]. During the compaction stage of scaffold fabrication, the SS316L/carbamide mixture must be consolidated under a sufficiently high pressure to attain the integrity of the green body, ready for subsequent processing steps. However, an excessively high compaction pressure can deform or even crush carbamide particles, adversely affecting pore morphology, interconnectivity, and overall scaffold performance [7]. Therefore, identifying an optimum compaction pressure is critical to preserving the desired pore geometry while ensuring adequate structural integrity.

Previous studies have proposed optimum compaction pressures for SS316L/carbamide mixtures over a broad range from 100 [11] to 500 MPa [12]. However, these recommendations were made without accounting for the compressive behavior of the powder mixture during compaction, leaving the critical pressure for carbamide particle deformation undefined. To address this gap, the present study examines the compression behavior of SS316L/carbamide mixtures with varied volume fractions of carbamide under uniaxial pressing. Load–displacement curves were analyzed to assess their compressibility and determine the critical compaction pressure at which carbamide particles begin to deform or fragment.

Materials and Method

Preparation of powder mixtures. A medical-grade SS316L powder (Wuxi Eternal Bliss Alloy Casting and Forging Co., China), exhibiting a spherical particle morphology as shown in Fig. 1(a), and a carbamide powder (Merck, Germany) with an ellipsoidal shape depicted in Fig. 1(b), were sieved through 200–300 mesh and 30–50 mesh screens, respectively. Particle morphology and sizes were analyzed using an optical microscope (Olympus, Japan) in combination with the ImageJ software to determine the average particle diameter (Dav). With this method, the average particle diameter of the SS316L powder was measured to be 29.7 ± 0.7 μm, while that of the carbamide powder was 532.2 ± 8.6 μm. To prevent particle agglomeration, a 3 vol% polyvinyl alcohol (PVA) binder solution was added to the SS316L and carbamide powders. The powders were then mixed using a tube roller mixer (KJMR II, China) for 2 h, with carbamide volume fractions set at 40%, 50%, and 60%.

Powder compaction. The SS316L/carbamide powder mixtures were cold-compacted using a die with an inner diameter of 12 mm. Prior to powder filling, the die inner surface was lubricated with a zinc stearate powder to minimize friction. A 7.5 g mixture of SS316L and carbamide powders was manually tapped into the die and compacted at room temperature *via* uniaxial pressing using a universal testing machine (Carson, Taiwan). The punch speed during both compression and decompression was maintained at 2 mm/min. To eliminate air from the powder bed and improve green density and strength, the mixture was pre-compressed at a load of 50 N before applying the main compaction pressure. Load–displacement data were recorded throughout the compaction process, with each powder mixture tested in four replicates to ensure reproducibility.

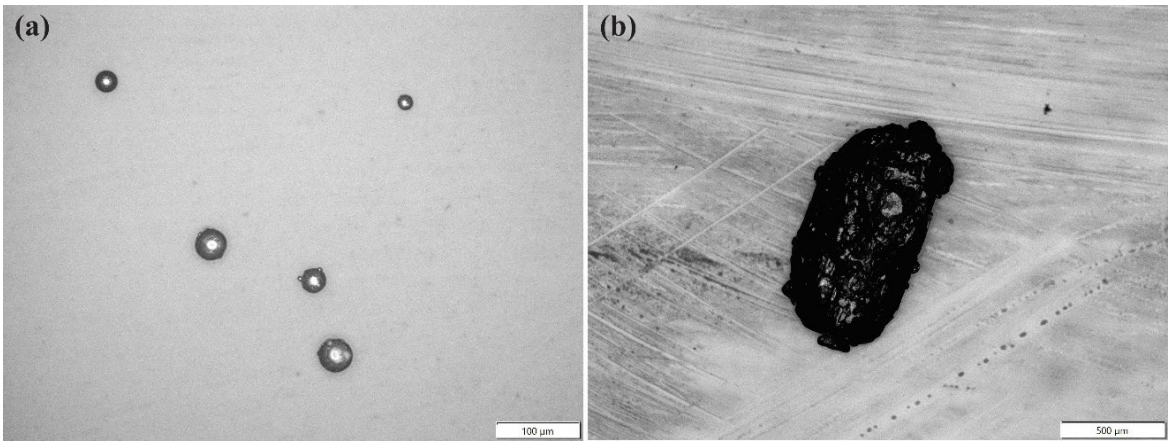

Fig. 1 (a) Medical grade SS316L powder particles and (b) a carbamide particle.

Analysis. The compression behaviors of SS316L, carbamide and their mixtures were analyzed based on the load-displacement plots obtained during compaction. To quantify the densification behavior, the Heckel model was employed to correlate the applied pressure with green density and then determine the optimum compaction pressure of SS316L/carbamide mixtures [13].

Specific net energy of powder compression. The specific net energy of powder compression ($E_{sp.net}$) was determined to quantify the energy required to initiate plastic deformation during the powder compaction process. The $E_{sp.net}$ was calculated as the difference between the specific energy required during powder compression ($E_{sp.cp}$) and the specific energy released during decompression ($E_{sp.ep}$) Eq. (1). The values of energy during compression ($E_{sp.cp}$) and during decompressioon ($E_{sp.ep}$) were obtained from the area under the loading–unloading curve.

$$E_{sp.net} = E_{sp.cp} - E_{sp.ep} \quad (1)$$

Elastic recovery. Elastic recovery describes the expansion of the powder bed during the decompression stage due to the release of compressive stresses. It can be determined using Eq. (2), where t_0 the final powder bed thickness after punch withdrawal and t_{min} represents the minimum powder bed thickness within the die cavity at the maximum compaction pressure.

$$ER = \frac{t_0 - t_{min}}{t_{min}} \quad (2)$$

Effective pressure. The pressure measured by the compaction machine, referred to as nominal pressure (P_n), does not accurately represent the actual pressure (P_a) within the die cavity. This discrepancy arises from the frictional forces between the punch and the die inner wall [14]. The value of P_a can be determined using Eq. (3), considering the friction coefficient (μ), die diameter (d), axial-to-radial pressure ratio (K), and the change in powder height (H) during compaction.

$$P_a = P_n \cdot \exp\left(-\frac{4K\mu H}{d}\right) \quad (3)$$

In this study, the value of K was assumed to be 1, considering that lubrication was applied to the die inner wall and the compaction process was carried out at a low speed. A moderate value of the friction coefficient ($\mu = 0.07$) was adopted to account for the effect of zinc stearate used as a lubricant [15].

The Heckel compaction model. The Heckel model describes powder densification during compression by treating pore reduction as a first-order kinetic process [13]. The final form of this model is presented in Eq. (4).

$$-\ln(1 - D) = KP + A \quad (4)$$

In this model, P is the actual compaction pressure (Pa), A represents the initial porosity of the powder bed, and D is the relative density reflecting the degree of densification. The linear region of the Heckel

plot is critical, since the inverse slope (K) provides the yield pressure (P_y), which indicates the onset of plastic deformation [4]. To improve the accuracy of the P_y value, a correction factor (R^2) was applied, and the final form of the model is expressed in Eq. (5).

$$P_y = R^2/K \tag{5}$$

where R^2 and K represent the correlation coefficient and the slope of the Heckel model linear regression plot, respectively [16]. The Heckel model also establishes an empirical correlation between the yield pressure (P_y) and the yield strength (σ_y), as expressed in Eq. (6).

$$P_y = 3\sigma_y \tag{6}$$

Results and Discussion

Load-displacement plots. Fig. 2(a) illustrates the load–displacement curves of SS316L/carbamide mixtures with varied carbamide volume fractions, indicating that the displacement during compaction increased with increasing carbamide volume fraction. This trend was attributed to the higher mechanical strength of SS316L particles, which acted as protective barriers, shielding carbamide particles from direct compressive forces. As the SS316L content decreased, this shielding effect was reduced, resulting in increased exposure of carbamide particles to pressure. Consequently, the carbamide underwent fragmentation, leading to a decreased in the overall powder bed height.

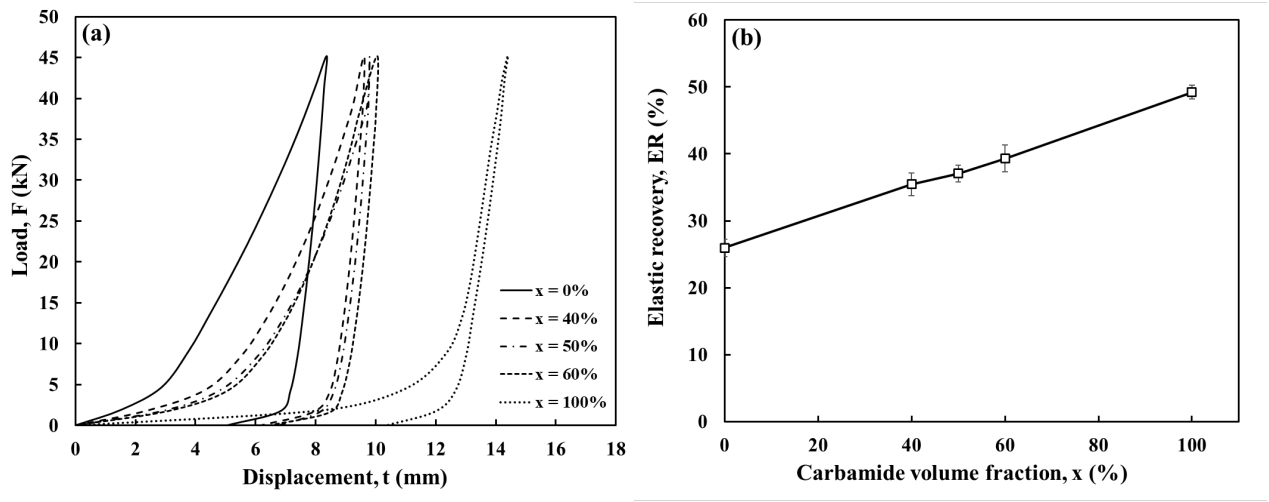

Fig. 2 (a) Load-displacement plots of SS316L/carbamide powder mixtures and (b) elastic recovery of SS316L/carbamide powder compacts.

Elastic Recovery. Fig. 2(b) illustrates the elastic recovery behavior of compacted SS316L/carbamide mixtures during decompression. The carbamide component exhibited greater elastic response compared to SS316L, reflecting its lower mechanical strength and higher deformability. As the carbamide content increased, interparticle cohesion within the compact decreased, resulting in enhanced overall elasticity of the SS316L/carbamide structure. This trend highlighted the influence of space holder volume fraction on the mechanical resilience and recovery characteristics of the composite compact.

Specific net energy. Compaction pressures ranging from 0 to 400 MPa were applied to the SS316L/carbamide powder mixtures using a universal testing machine. Load–displacement data from a single compaction cycle were analyzed using Eq. (3) to determine the actual pressure within the die cavity, which was found to range between 0 and 275 MPa. The relationship between energy and pressure is illustrated in Fig. 3(a), while Fig. 3(b) presents a comparison between the experimentally obtained specific net energy and the values predicted by the rule of mixtures (ROM), as described in Eq. (7).

$$\left(\mathrm{E_{sp.net}}\right)_{\mathrm{mix}} = (1-\mathrm{x})\left(\mathrm{E_{sp.net}}\right)_{\mathrm{SS}} + \mathrm{x}\left(\mathrm{E_{sp.net}}\right)_{\mathrm{Carb}} \quad (7)$$

With compaction pressure increasing from 0 to 275 MPa, the specific net energy ($E_{sp.net}$) of the x = 0% mixture increased most sharply, indicating substantial energy absorption due to the plastic deformation of SS316L particles. For mixtures with x = 40–60% carbamide, $E_{sp.net}$ continued to rise with increasing pressure but at a reduced slope, as part of the energy was dissipated through the fracture of more brittle carbamide particles. As the carbamide content increased further, $E_{sp.net}$ declined, reflecting less efficient compaction. In the x = 100% mixture, $E_{sp.net}$ remained low and nearly constant even at higher pressures, consistent with the fragile nature of carbamide, which tends to fracture rather than undergoing plastic deformation. These findings demonstrated that the carbamide volume fraction critically influenced both the energy efficiency of compaction and the dominant deformation mechanism. The optimum range was observed at 40–50% carbamide, where SS316L contributed to plastic deformation while sufficient porosity was retained for scaffold functionality.

The rule of mixtures (ROM) effectively predicted a linear decrease in specific net energy with increasing volume fraction of carbamide. While the experimental data generally followed this trend, notable deviations were observed at higher compaction pressures. At low pressures (25–75 MPa), the experimentally determined energy values closely aligned with ROM predictions, as shown in Fig. 3(a), where compaction was primarily governed by particle rearrangement. However, at elevated pressures (125–275 MPa), significant deviations emerged, particularly in mixtures containing 40–60% carbamide, due to nonlinear effects associated with SS316L plastic deformation and carbamide particle fracture. These findings highlighted the limitations of ROM under high-pressure conditions and underscored the complex interplay between constituent materials during compaction.

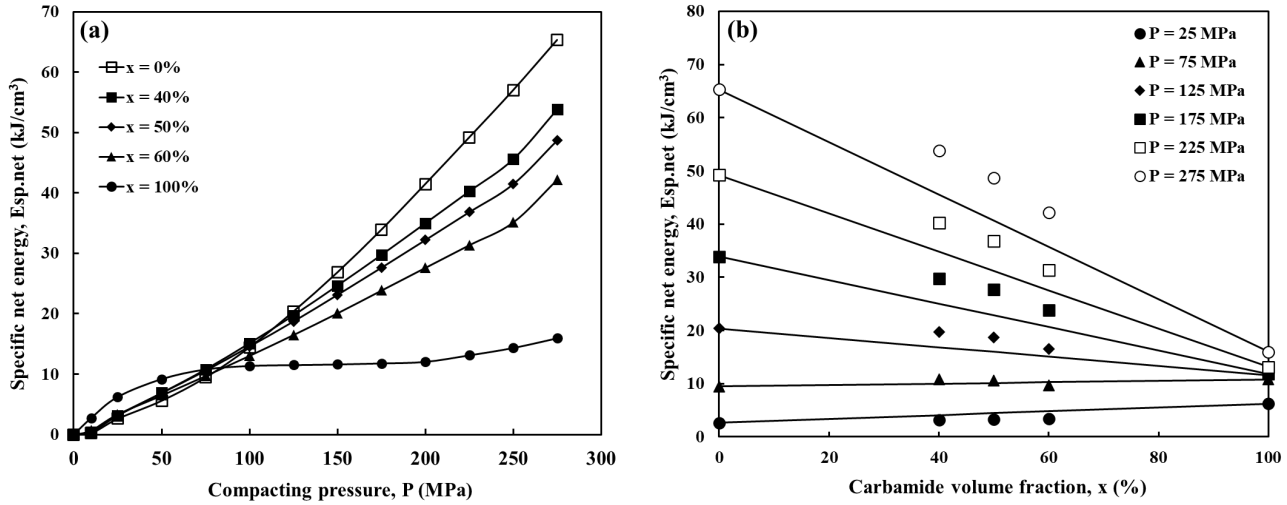

Fig. 3 (a) Specific net energy ($E_{sp.net}$)-pressure relationship for the compaction of SS316L/carbamide powder mixtures and (b) comparison between experimentally determined and predicted specific net energy ($E_{sp.net}$) values.

Relative density. The experimentally acquired relative-density data shown in Fig. 4 formed the primary basis for the Heckel analysis of powder densification during compaction. For the x = 0% composition (monolithic SS316L), the relative density (D) was initially low at low pressures and increased gradually with increasing pressure. In contrast, the mixtures containing x = 40–60% carbamide exhibited higher initial D and steeper increases, attributed to carbamide particles promoting early pore filling. At x = 100%, D was already very high at low pressures, primarily due to carbamide fragmentation, which filled voids, rather than being due to plastic deformation. Based on these observed trends, Heckel fitting was performed over the pressure range of 0–275 MPa for compositions of x = 0–60%. For x = 100%, a reduced range of 0–25 MPa was applied to exclude the fragmentation-dominated regime where the assumptions underlying the Heckel model were no longer valid.

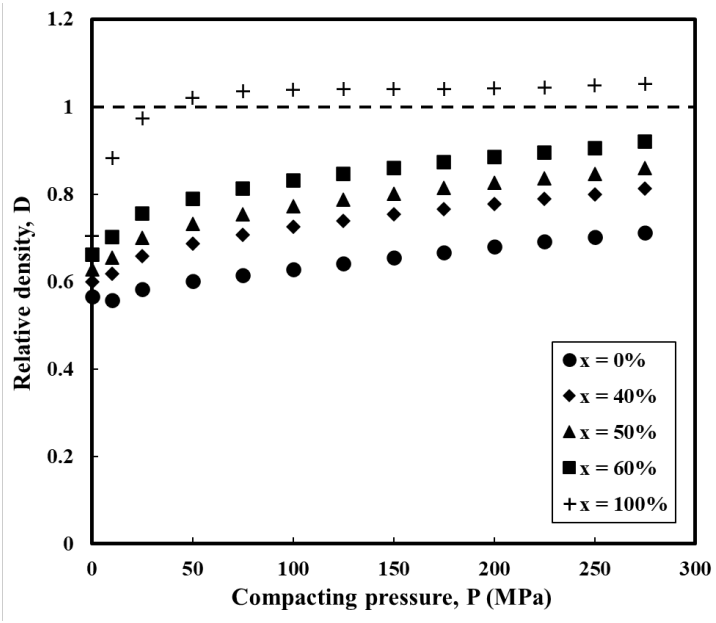

Fig. 4 At-pressure relative density values of SS316L/carbamide powder mixtures.

Heckel model compaction. Fig. 5(a) presents the plots of $-\ln(1-D)$ *versus* compaction pressure (P) for five carbamide volume fractions (x = 0, 40, 50, 60, and 100%), with linear fittings applied within the selected pressure range. The results clearly show that the slope increased with the rise of carbamide content, where the lowest slope was obtained at x = 0% and the highest at x = 100%. This indicated that the mixtures with higher volume fractions of carbamide required lower applied pressures to reach the yield pressure (Py), which represented the onset of plastic deformation during compaction. For x = 100%, the slope was steep even at very low pressures, reflecting the brittle fragmentation and rapid pore filling by broken carbamide particles rather than plastic deformation. In contrast, for x = 0% (SS316L), densification proceeded relatively fast in the low-pressure range (0–25 MPa) due to particle rearrangement, but slowed down significantly at higher pressures (25–275 MPa) where the dominant mechanism was the elastic–plastic deformation of metallic particles. Intermediate carbamide contents (x = 40–60%) exhibited faster densification at low pressures (0–25 MPa), as carbamide particles facilitated the filling of interparticle voids during the rearrangement stage. At higher pressures (25–275 MPa), however, a combined mechanism occurred, consisting of elastic–plastic deformation of SS316L powder particles together with carbamide fragmentation. This combined mechanism produced steeper slopes compared to x = 0%, thereby yielding lower Py values than SS316L alone.

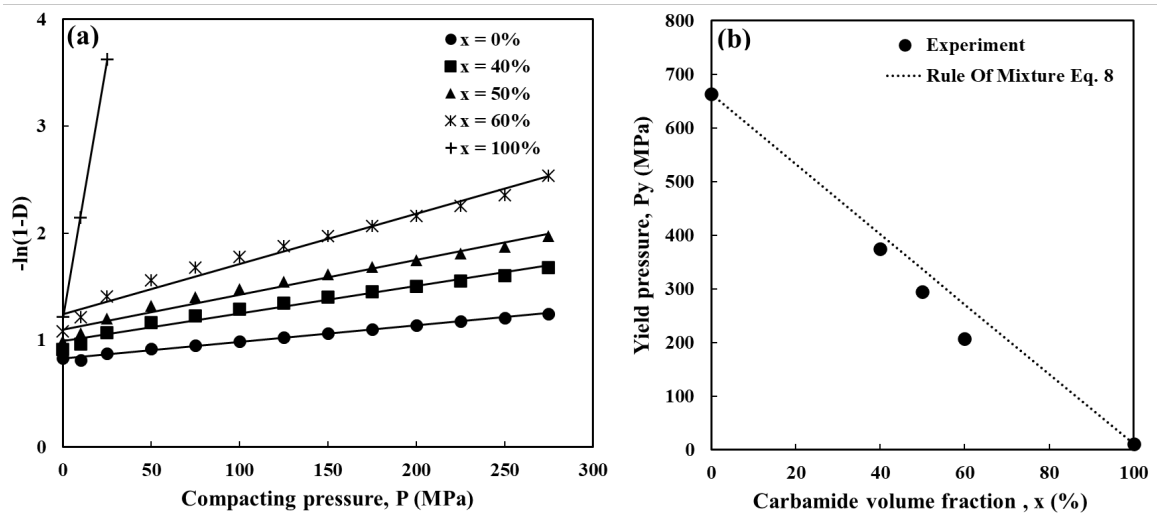

Fig. 5 (a) Fitting of data plots into the Heckel compaction model and (b) comparison between experimentally determined and predicted specific yield pressure (P_y) values.

Table 1 summarizes the regression coefficients (R^2) and yield pressures (P_y) obtained from the Heckel plots in Fig. 5(a). For x = 0–60%, linear fitting was performed over the pressure range of 25–275 MPa, while for x = 100% the fitting range was limited to 0–25 MPa. The results showed that all the compositions exhibited high R^2 values, confirming the statistical reliability of the linear fits. The general trend (x = 0–60%) showed a decrease in P_y with increasing carbamide volume fraction, indicating that the yield pressure was reached at lower stresses when brittle carbamide particles were present. This behavior appeared due to the fragmentation of carbamide particles and pore filling by fragmented carbamide particles, which facilitated densification compared to pure SS316L that required higher pressures for plastic deformation. The P_y value for x = 100% was extremely low (10.35 MPa), differing by an order of magnitude from x = 0–60%. This reflected the brittle fragmentation and rapid pore filling by carbamide particles occurring at low compaction pressures. At x = 0% (pure SS316L), the compaction behavior was governed by particle rearrangement at low pressures (0–25 MPa), followed by elastic–plastic deformation in the intermediate to high pressure range (25–275 MPa). The applied pressure was insufficient to induce fragmentation of SS316L particles and thus densification was primarily controlled by the plastic deformation of the metallic phase. The yield pressure value obtained for SS316L was considered reliable, as the yield strength (σ_y) calculated from Eq. (6) was 221 MPa, which lies within the ASTM A276 specified range for SS316L (170–310 MPa) [17].

Fig. 5(b) presents a comparison between the experimental P_y values and the predictions from the rule of mixtures (ROM) based on Eq. (8). The ROM prediction showed increasing deviations with higher carbamide volume fractions. This deviation was attributed to the nonlinear mechanisms (elastic–plastic deformation and fragmentation) that occurred during the compaction process of SS316L and carbamide mixtures.

$$\left(\mathrm{P_y}\right)_{\mathrm{mix}} = (1-\mathrm{x})\left(\mathrm{P_y}\right)_{\mathrm{SS}} + \mathrm{x}\left(\mathrm{P_y}\right)_{\mathrm{Carb}} \tag{8}$$

Table 1. Yield pressure (P_y) values of SS316L/carbamide mixtures from Heckel plot analysis.

Carbamide volume fraction x [%]	Min pressure range covered [MPa]	Min pressure range in linier region [MPa]	Coefficient of correlation R^2	Yield pressure P_y [MPa]
0	0-275	25-275	0.9944	662.93
40	0-275	25-275	0.9745	374.81
50	0-275	25-275	0.9714	294.36
60	0-275	25-275	0.9739	207.21
100	0-25	0-25	0.9997	10.35

Fig. 6 illustrates the characteristics of the green bodies. Fig. 6(a) shows the green body with x = 60% compacted at 275 MPa, which exceeded the *Py* value listed in Table 1. In contrast, Fig. 6(b) presents the green body with x = 50% compacted at 275 MPa, which was lower than the corresponding *Py* value in Table 1. From these images, it could be seen that in the sample shown in Fig. 6(a), a large fraction of carbamide particles had undergone fragmentation, losing their initial elliptical morphology. The resulting carbamide fragments filled smaller pores, forming highly irregular pore interconnectivity. In the sample shown in Fig. 6(b), however, the majority of carbamide particles largely retained their original elliptical shape. The limited fragmentation of carbamide in this green body was expected to facilitate a more favorable pore structure and final pore interconnectivity.

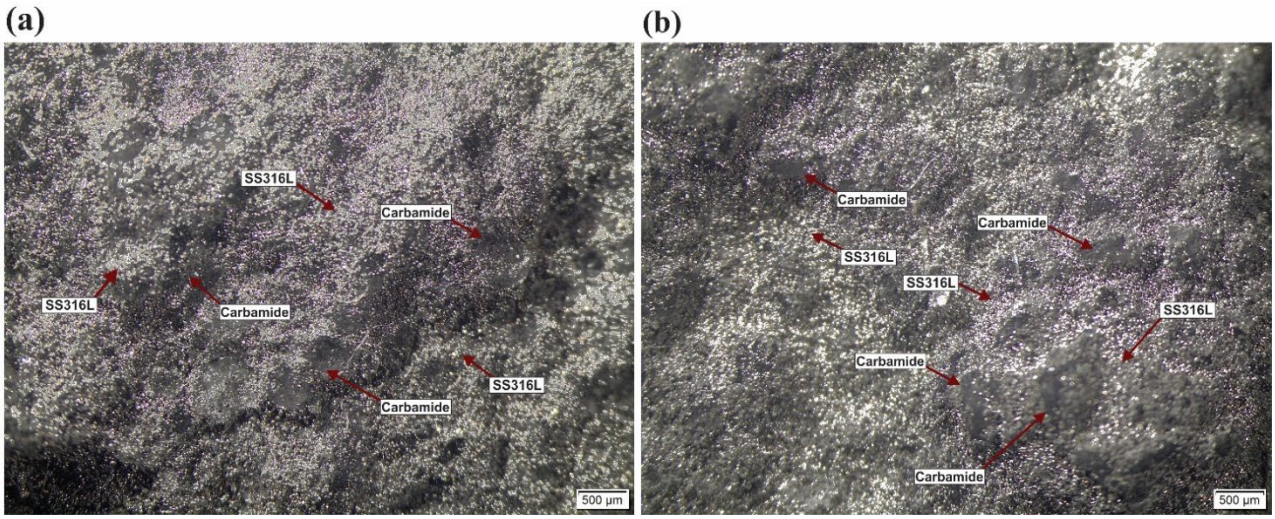

Fig. 6 Characteristics of the green bodies with two different volume fractions: (a) x = 60% and P = 275 MPa (b) x = 50% and P = 275 MPa.

Conclusions

This study examined the compaction behavior of SS316L/carbamide powder mixtures in scaffold fabrication by using the space holder method. Uniaxial pressing experiments were performed with volume fractions of carbamide ranging from 0 to 100%, and the compaction behavior was analyzed through load–displacement plots, elastic recovery, specific net energy ($E_{sp.net}$), relative density, and the Heckel model.

The results indicated that a higher carbamide volume fraction increased displacement and elastic recovery due to the brittle nature of carbamide and reduced interparticle cohesion, while simultaneously lowering $E_{sp.net}$ as plastic energy absorption becomes less efficient. At intermediate fractions (40–50%), $E_{sp.net}$ was maximized, as the plastic deformation of SS316L was complemented by carbamide-induced porosity retention. Relative density trends confirmed that carbamide promoted early densification *via* fragmentation and pore filling, while SS316L required higher pressures to undergo plastic deformation.

The Heckel analysis showed a decrease in yield pressure (P_y) with increasing carbamide volume fraction, reflecting easier densification in carbamide-rich mixtures. In addition, P_y for 100% carbamide (~10 MPa) clearly represented the characteristics of brittle carbamide. Comparison with the rule of mixtures predictions highlighted significant deviations at high carbamide volume fractions, driven by nonlinear mechanisms of SS316L plasticization and carbamide fracture. Microstructural observations further validated these findings, showing that compaction above P_y caused severe carbamide fragmentation and irregular pore connectivity, whereas compaction below P_y preserved particle morphology and pore characteristics. The optimum compaction window was identified at 40–50% carbamide volume fraction under pressures near P_y, offering the best balance between structural integrity and controlled porosity for scaffold applications.

Acknowledgements

This research was funded through a research grant from the Department of Mechanical and Industrial Engineering, Faculty of Engineering, Universitas Gadjah Mada, under contract number 1610402/UN1.FTK/SK/HK/2025.

References

[1] J. Fan, J. Xu, X. Wen, L. Sun, Y. Xiu, Z. Zhang, T. Liu, D. Zhang, P. Wang, D. Xing, The future of bone regeneration: Artificial intelligence in biomaterials discovery, Mater. Today Commun. 40 (2024) 109982.

[2] N. Aslan, B. Aksakal, F. Findik, Fabrication of porous-Ti6Al4V alloy by using hot pressing technique and Mg space holder for hard-tissue biomedical applications, J. Mater. Sci. Mater. Med . 32(7) (2021) 80.

[3] B. Arifvianto, M. A. Leeflang, J. Zhou, Diametral compression behavior of biomedical titanium scaffolds with open, interconnected pores prepared with the space holder method, J. Mech. Behav. Biomed. Mater. 68 (2017) 144-154.

[4] B. Arifvianto, M. A. Leeflang, J. Zhou, The compression behaviors of titanium/carbamide powder mixtures in the preparation of biomedical titanium scaffolds with the space holder method, Powder Technol. 284 (2015) 112-121.

[5] B.Q. Li, R.Z. Xie, X. Lu, Microstructure, mechanical property and corrosion behavior of porous Ti–Ta–Nb–Zr, Bioact. Mater. 5 (2020) 564-568.

[6] A. Rodriguez-Contreras, M. Punset, J. A. Calero, F. J. Gil, E. Ruperez, J. M. Manero, Powder metallurgy with space holder for porous titanium implants: A review, J. Mater. Sci. Technol. 76 (2021) 129-149.

[7] B. Arifvianto, J. Zhou, Fabrication of metallic biomedical scaffolds with the space holder method: A review, Mater. 7 (2014) 3588-3622.

[8] M. Mirzaei, M. H. Paydar, Fabrication and Characterization of Core–Shell Density-Graded 316L Stainless Steel Porous Structure, J. Mater. Eng. Perform. 28 (2019) 221-230.

[9] Z. Abdullah, S. Ahmad, A. Ismail, N. Ahmed Khan, Processing of porous stainless steel by compaction method using egg shell as space holder, Key Eng. Mater. 791 (2018) 123-128.

[10] H. Jain, D. P. Mondal, G. Gupta, R. Kumar, S. Singh, Synthesis and characterization of 316L stainless steel foam made through two different removal process of space holder method, Manuf. Lett. 26 (2020) 33-36.

[11] H. I. Bakan, A novel water leaching and sintering process for manufacturing highly porous stainless steel, Scr. Mater. 55 (2006) 203-206.

[12] H. Jain, G. Gupta, R. Kumar, D. P. Mondal, Microstructure and compressive deformation behavior of SS foam made through evaporation of urea as space holder, Mater. Chem. Phys. 223 (2019) 737-744.

[13] R. W. Heckel, Density-Pressure Relationships in Powder Compaction, Trans. Metall. Soc. AIME. 221 (1961) 671-675.

[14] S. T. Hong, Y. Hovanski, C. A. Lavender, K. S. Weil, Investigation of die stress profiles during powder compaction using instrumented die, J. Mater. Eng. Perform. 17(3) (2008) 382-386.

[15] R. F. Mallender, C. J. Dangerfield, D. S. Coleman, Friction coefficients between iron powder compacts and die wall during ejection using various admixed zinc stearate lubricants, Powder Metall. 15 (1972) 130-152.

[16] J.M. Sonnergaard, A critical evaluation of the Heckel equation, Int. J. Pharm. 193(1999)63-71.

[17] ASTM Internasional, Standard Specification for Stainless Steel Bars and Shapes, ASTM A276-06. 2006.

The publication of this article was funded by the Delft University of Technology 10.13039/501100001831